Simulations of Edge Configurations in Quasi-Helically Symmetric Geometry using EMC3-EIRENE

A. Bader (1), D.T. Anderson (1) C.C. Hegna (1), Y. Feng (2), J.D. Lore (3), J.N. Talmadge (1)

1) University of Wisconsin, Madison, WI, USA 2) Max-Planck Institut für Plasmaphysik, Greifswald, Germany 3) Oak Ridge National Laboratory, Oak Ridge, TN, USA

Simulations of the edge of a Quasi-Helically Symmetric (QHS) stellarator with geometry based on the Helically Symmetric eXperiment (HSX) are performed using the coupled codes EMC3-EIRENE. The standard configuration of HSX has an island structure outside the separatrix, corresponding to the 8/7 resonance. In addition to the standard configuration, two other configurations are examined: one with small islands outside the separatrix corresponding to the 16/15 resonance, and one with large islands corresponding to the 4/4 resonance. Using EMC3-EIRENE, density scans are employed, while scaling input power linearly with density, in order to determine the transition point from a low to a high recycling regime. The small island and the standard cases show markedly similar behavior, but the large island configuration transitions to high-recycling and detached regimes at significantly lower plasma densities. Reducing the perpendicular viscosity creates behavior more consistent with 2-point model predictions by reducing the role of perpendicular transport through edge islands and reducing friction loss from counter-streaming parallel flows. When carbon impurities are added, the large island configuration exhibits a large increase in radiated power, while the two configurations with smaller islands do not.

I. INTRODUCTION

Controlling the plasma edge is critical for the successful operation of next-step stellarator devices. The edge needs to provide a large enough temperature gradient between the targets and the last closed flux surface (LCFS) of the plasma to protect the plasma facing components from melting and to protect the confined plasma from impurities and cold neutrals entering from the edge. These requirements necessitate the move to diverted plasmas [1, 2]. However stellarator divertors are not as straightforward as tokamak divertors and may take various forms such as island divertors in W7-AS [3] and W7X [4], and the Helical Divertor [5] and Local Island Divertor configurations in LHD [6]. Simulation capabilities from the coupled codes EMC3-EIRENE have been developed to assist in determining the relevant physics in the fully 3D stellarator geometries [7].

This work represents the first dedicated study of the edge properties of quasi-helically symmetric (QHS) configurations through numerical simulations using EMC3-EIRENE. Different divertor operating regimes on geometries found in the Helically Symmetric eXperiment (HSX) Stellarator [8] are explored. In order to examine divertor regimes of interest, a fictional device is considered that has the HSX magnetic geometry, but is capable of confining much hotter and denser plasmas than are currently available in the experiment. Of particular interest to edge physics in stellarators is the transition from low recycling to high recycling and detached divertor regimes. Islands in the edge may support counter-streaming flow structures. These are posited to modify the momentum balance by introducing additional friction forces, preventing attainment of a high recycling regime [9]. The effects of edge islands and the resulting flow structures on the transition to the high recycling and detached regimes is a major focus area in stellarator edges and this paper. Specifically, several magnetic configurations with different edge properties are considered. The configurations differ in the magnetic island structures in the edge and allow for the investigation of the effect of island number and size on edge physics. Additionally, comparisons are made between a normal sized device and one with double-size. Increasing the device size, increases the perpendicular distance between the counter-streaming flow structures, thus modifying momentum balance. A consequence of the increased perpendicular distance is a reduction of friction from the counter-streaming flows allowing for the attainment of a high-recycling regime, as predicted for W7X [10] and for some of the configurations explored in this paper.

Simulation work by Feng et al suggests that in stellarator configurations, energy balance along a field line can be described by [10],

$$T_u^{7/2} = T_d^{7/2} + \frac{7}{2}\frac{q_\parallel L}{\kappa_e} - \frac{7\chi\,(n_u + n_d)}{4\kappa_e \Theta^2}\,(T_u - T_d)\,. \tag{1}$$

Here, T_u and n_u represent the temperature and density at the separatrix or upstream, T_d and n_d represent the target or downstream temperature and density, L is the length along a field line between upstream and downstream points, and κ_e is the parallel electron thermal conductivity. The parallel heat flux, $q_\parallel$, is given by,

$$q_\parallel = \gamma n_d T_d c_s, \tag{2}$$

where γ is a constant representing the sheath power transmission coefficient, n_d is the downstream density, and c_s is the sound speed. The final term on the right hand side of 1, accounts for the competition between cross-field transport and equilibration processes along a field line, through a magnetic pitch parameter Θ. For tokamaks, Θ is defined as

the ratio of the poloidal to toroidal field strengths and typically has values in the edge of about 0.1 - 0.2. However, for stellarators, Θ represents the ratio of the resonant radial field to the background field and can be significantly lower, reaching values of $\sim 10^{-3}$ for W7-AS. Therefore the additional term is usually neglected in tokamaks, but plays a much larger role in stellarators. This additional term accounts for finite perpendicular transport processes with the perpendicular thermal diffusivity given by $\chi = \chi_e + \chi_i$. Low values of χ should result in a more tokamak-like behavior.

Stellarator edges typically have complicated 3D field structures containing both stochastic regions and magnetic islands. Connection lengths can vary greatly from short lengths in the stochastic region to infinite lengths for confined field lines inside islands. Due to the presence of long connection lengths, and the proximity of field lines with widely varying connection lengths, perpendicular transport processes are posited to play an important role [9].

If the last term on the right hand side of 1 is removed, the standard description of the "2-point model" is recovered [11]. The 2-point model can be used to distinguish between low recycling and high recycling regimes. In the low recycling regime, the thermal conductivity is greater than the product of the parallel heat flow and the connection length, $\kappa_e T^{7/2} \gg (7/2) q_\parallel L$. In this case, the upstream temperature, T_u is roughly equivalent to the downstream temperature, T_d. The high recycling regime corresponds to the opposite limit with $\kappa_e T^{7/2} \ll (7/2) q_\parallel L$. In this limit, there is a difference between T_u and T_d, as indicated in Eq. 1. Thus, there is a limitation to how much parallel heat the plasma can conduct to the divertor targets, hence the alternate name, 'conduction-limited regime'.

Using Eqs. 1 and 2, along with $p_u = 2p_d$, one can derive a relationship between the upstream and downstream densities in the low and high recycling regime limits. In the low recycling regime, where $T_d \approx T_u$, the densities scale linearly with $n_d \propto n_u$. In the high recycling regime, $n_d \propto n_u^3 q_\parallel^{-8/7}$, the edge density increases as the cube of the separatrix density. The point where the downstream density changes from a linear to a cubic relationship with increasing plasma density can be viewed as the onset of the high recycling regime [12]. Additional losses of momentum, possibly from neutral interactions or flow effects from islands can cause deviations to the two-point model. This paper focuses mainly on the latter cause. The high recycling regime is desirable for operation because of the reduction of T_d. If T_d is Maxwellian and significantly below the physical sputtering limit for the wall material, there will be a significant reduction in both impurity generation and wall erosion. Also the increase in density leads to an increase in edge radiation, providing a more even distribution of power to the wall.

If the density at the target plates gets high enough, or enough momentum is lost from other sources, the plasma can lose all its energy through interactions with plasma ions, neutrals and impurities before reaching the target. In

this case, all energy is radiated, and the plasma enters a "detached" regime. While this may seem advantageous for reactor operation, since power is being uniformly radiated by the neutrals, it is difficult, but not impossible, to maintain density control in the detached regime in both stellarators and tokamaks [13].

The regimes of divertor operation have been well-studied on tokamaks [12, 14], but have only garnered attention recently in stellarators. Results from divertor experiments on W7-AS and LHD showed an absence of a high recycling regime and a direct transition to a detached regime [3, 15, 16]. Early modeling showed the need to include cross-field transport, because diffusion through island structures may compete with parallel transport around island edges. Also, modeling indicated that momentum balance along the field line was being affected by friction from counter-streaming flows [9].

Because of the Bohm condition at the wall, strong parallel flows arise in the ionization region of both stellarators and tokamaks. In tokamaks the flows are oppositely directed on the inner and outer divertor strike points. However, the legs are generally well separated by the private-flux region and the flows do not interact. However, the case is different in stellarators with island structures located near the wall. Flows arising on either side of the island are oppositely directed and can interact with each other and with flows in adjacent islands. The adjacent islands can either be members of the same poloidal chain, as is usual in W7-AS and W7X, or of a radially separated island chain with a different poloidal mode number, as is the case in LHD.

Cross-field transport effects are usually negligible in tokamaks with respect to equilibration processes along a field line, but they do play a role in the calculation of λ_{SOL}, the scrape-off layer width. Small values of χ imply that heat from the plasma is confined to a very small λ_{SOL} outside the separatrix. This impacts the width of the heat flux channel to the divertor. A global λ_{SOL} is harder to define for a stellarator. It is possible to define an analogous value, $\lambda_{\mathrm{SOL,Isl}}$ to describe the behavior for the island scrape-off layer, the region that arises when a divertor plate is inserted into an edge island. However, this is of limited utility for the general stochastic edge case. Nevertheless, a similar gross behavior may be observed in all stellarator geometries when considering the heat flux deposition onto the wall. Smaller values of χ lead to flux being concentrated over a smaller local area. Increasing χ will lead to a widening of the flux channel. It should be noted that χ values are not well known in either tokamak or stellarator edges. Furthermore, they may be affected by turbulent transport phenomena and may vary in both space and time. Predictions of λ_{SOL}, particularly on ITER, are an open field of research [17, 18]. The effects of varying both D and χ are discussed later in this paper, but a calculation of their values from first principles is beyond the scope of the paper.

It may be possible to operate a reactor-relevant diverted stellarator in the detached regime if it can be operated stably or in the high recycling regime if it is obtainable. A detached regime can only be stable if the neutrals are prevented from entering the separatrix. If neutral penetration into the core plasma is high, it will lead to a loss of density control and radiative collapse [19]. Unfortunately, it is not possible to fully model the stability of any operating regime in EMC3-EIRENE, and stability analysis is beyond the scope of this paper. However, the role that impurities play in transitioning from a high (or low) recycling regime to a detached regime are examined.

The layout of the rest of the paper is as follows. Section II introduces the EMC3 code that is used for the analysis. Section III introduces the HSX device and discusses three separate magnetic configurations that are used for the simulations. Section IV provides the results indicating the transitions from a low recycling to a high recycling regime. The roles played by perpendicular transport coefficients and parallel viscosity are also discussed. Additionally it touches on the transition into a detached regime through the addition of a carbon impurity. Section V summarizes the paper and describes future work.

II. EMC3-EIRENE MODEL

To model the HSX plasma, the Edge Monte Carlo code EMC3 is coupled with the neutral transport code EIRENE. EMC3 solves for plasma properties in a user-supplied magnetic mesh representing a fully 3D geometry. This geometry can include both open field lines that terminate on target surfaces, and closed field lines that exist inside the plasma core and in closed islands. Thus it is ideal for use in the complicated 3D geometries found in stellarators. Particle following is accomplished by a novel reversible field line mapping technique [20].

EMC3 solves for the plasma temperature and density profiles in the arbitrary magnetic geometry using locally field-aligned fluid equations (see Eqs. 3–6)[7]. The magnetic grid is pre-computed, and does not evolve through plasma effects. EIRENE handles neutrals that are recycled at target-plasma interfaces or neutrals that are sourced through gas puffs or neutral beams. EMC3-EIRENE has previously been used to model edge parameters on the stellarators W7-AS, W7X and LHD [9, 16, 21]. It has also been used to model the 3-D edges that occur when resonant magnetic perturbation coils are used on tokamaks [22–25].

EMC3 solves for the following field-aligned fluid equations,

$$\nabla \cdot \left(n_i V_{i\parallel} \vec{b} - D_i \vec{b_\perp} \vec{b_\perp} \cdot \nabla n_i \right) = S_p, \tag{3}$$

$$\nabla \cdot \left(m_i n_i V_{i\parallel} V_{i\parallel} \vec{b} - \eta_\parallel \vec{b}\vec{b} \cdot \nabla V_{i\parallel} - \mu_\perp \vec{b}_\perp \vec{b}_\perp \cdot \nabla m_i n_i V_{i\parallel} \right) = -\vec{b} \cdot \nabla p + S_m, \tag{4}$$

$$\nabla \cdot \left(\frac{5}{2} n_e T_e V_{i\parallel} \vec{b} - \kappa_e \vec{b}\vec{b} \cdot \nabla T_e - \frac{5}{2} T_e D_i \vec{b_\perp} \vec{b_\perp} \cdot \nabla n_e - \chi_e n_e \vec{b_\perp} \vec{b_\perp} \cdot \nabla T_e \right) = -k \left(T_e - T_i \right) + S_{ee}, \tag{5}$$

$$\nabla \cdot \left(\frac{5}{2} n_i T_i V_{i\parallel} \vec{b} - \kappa_i \vec{b}\vec{b} \cdot \nabla T_i - \frac{5}{2} T_i D_i \vec{b_\perp} \vec{b_\perp} \cdot \nabla n_i - \chi_i n_i \vec{b_\perp} \vec{b_\perp} \cdot \nabla T_i \right) = +k \left(T_e - T_i \right) + S_{ei}. \tag{6}$$

Eq. 3 represents the conservation of mass, Eq. 4 represents the conservation of momentum along $\vec{b}$, and Eqs. 5 and 6 represent the conservation of energy for electrons and ions respectively. $\vec{b}$ is the unit vector along the magnetic field and $\vec{b_\perp}\vec{b_\perp} = \overleftrightarrow{I} - \vec{b}\vec{b}$. The perpendicular transport parameters. D_i, χ_i, and χ_e represent the cross-field particle diffusion, the thermal diffusivity for ions and the thermal diffusivity for electrons, respectively. The perpendicular transport parameters are user-supplied and global, so that they represent a single value over the entire computational domain. $V_{i\parallel}$ is the parallel ion velocity, $\mu_\perp$ is the perpendicular viscosity, $\eta_\parallel$ is the parallel Braginskii viscosity, and $k = 3 n_e \nu_e m_e / m_i$. In EMC3, $\mu_\perp = D_i$ for simplicity. (From here forward, we drop the subscript i when referring to D.) For all calculations presented here, $\chi_i = \chi_e = 3D$. The four source terms, S_p, S_m, S_{ee}, and S_{ei} represent the particle, momentum and energy sources from neutrals. In addition the energy source from electrons can also include losses from impurity radiation (see Section IV C).

EMC3-EIRENE solves for equilibrium through an iteration scheme, solving for momentum, energy and neutral transport separately. For the simulations in this paper a simulation is converged in a statistical sense if the absolute differences between one iteration and several preceding ones are below 2%. This can take anywhere from 30 to 100 iterations.

In order to make simulations over the fully 3-D regions tractable, EMC3 makes a number of assumptions about the plasma model in the edge. No perpendicular flows are allowed and hence, cross-field effects are solely controlled by the user defined diffusion coefficients. The equilibrium magnetic field is fixed throughout the simulations. No finite-β or flow induced changes to magnetic structures are allowed, despite that these are known to affect core resonant islands [26, 27]. All cross-field transport coefficients are constant throughout the computational domain with no distinction made between the confinement region and the edge. Interior boundary conditions are generally defined on a topologically toroidal magnetic structure in the plasma confinement region, usually close to the separatrix. Power flow through this surface is proscribed along with the plasma density at the surface. The outer boundary is

determined either by material walls or a vacuum region. A Bohm boundary condition is required for the parallel flow at the material walls. In the simulations in this paper, the domain extends out to the vessel wall in all directions, so there are no vacuum regions present.

III. THE HSX STELLARATOR AND ITS MAGNETIC GEOMETRY

The geometry of the Helically Symmetric eXperiment (HSX) is chosen in order to examine edge properties for possible next step stellarator devices with quasi-helical symmetry (QHS). HSX is a stellarator with four periods, major radius of ∼1.2 m and minor radius ∼0.12 m. In this paper, many of the simulations use a "double-size" HSX, in which all physical dimensions are multiplied by 2. However, some results from the normal size HSX are included for comparison. In the standard configuration, the rotational transform varies from 1.04 at the center to 1.2 at the edge. Also in this configuration the LCFS is bounded by a magnetic island chain with toroidal number ($n = 8$) and poloidal number ($m = 7$) that is resonant at the 8/7 surface outside the confinement region, island chain. Because some of these islands intersect the vessel wall, it is possible to consider HSX as having an unoptimized island divertor or "natural divertor." It is considered unoptimized because currently there is no divertor structure, either physical or magnetic, to guide the plasma flux to specific places on the vessel in order to either maximize the plasma wetted area on targets, or direct it to specific locations.

In order to model the edge plasma with EMC-EIRENE, a fairly comprehensive magnetic grid is required for the entire 3D edge region in the simulation domain. HSX has four field periods, each of which possess typical stellarator symmetry in that the coils are mirrored in the toroidal (ϕ) direction about the midpoint, with Z being replaced with $-Z$ in the mirrored half (Here R, ϕ, Z refers to cylindrical coordinates). The grid is generated by starting with a mesh of points on one toroidal slice. These points are then followed along field lines in order to generate grids at other toroidal values. In this way the code can easily advance particles along field lines using the reversible field line mapping and does not require any field line calculations after the grid has been generated. From geometrical considerations, it is sufficient to model a toroidal region spanning $\pi/4$ radians and invoke stellarator symmetry at either boundary. Field following for these simulations uses only vacuum fields, however any magnetic field that satisfies $\nabla \cdot \vec{B} = 0$ throughout the domain can be used.

As a grid is moved toroidally along field lines, it deforms due to magnetic shear. Shear in the edge of all the HSX geometries in this paper is mostly small. However, in the unconfined plasma, gross deformation can be produced over short toroidal transits. These deformities impose a limit to how far toroidally a grid can be moved. For HSX,

the grids can be moved along field lines toroidally about $\pi/40$ radians, after which they exhibit large deformities in specific areas. To accommodate this limitation the full $\pi/4$ simulation domain is broken up into 5 toroidal zones, each spanning $\pi/20$ radians. Grids are generated at the center of each region, at locations $\pi/40$, $3\pi/40$, $5\pi/40$, $7\pi/40$, and $9\pi/40$. As mentioned above, at 0 and $\pi/4$, stellarator symmetry is invoked. At the interfaces located at, $2\pi/40$, $4\pi/40$, $6\pi/40$, and $8\pi/40$, the particles are mapped across the zone boundary. Grid resolution at these boundaries determines the errors for particle following.

Because the edge region is the area of focus for this paper, for computational reasons, the grid does not extend deep into the confined region of the plasma. Therefore, there is an innermost flux surface that is very close to the separatrix. The density and input power to electrons and ions at a specific flux surface is set by the user, and EMC3 calculates the appropriate recycling flux so that the density is maintained at this surface.

HSX is surrounded by a vessel of roughly the same shape as the LCFS in the standard configuration. The experimental device has various diagnostics protruding from the vessel wall that effectively serve as limiting devices in the edge, but these structures are not included in this paper for simplicity. In order to properly model the HSX geometry, the magnetic grid extends beyond the wall throughout the entire computational domain. Cells behind the wall are treated as target cells and serve as both plasma sinks and sources for recycling and reflected neutrals. The grid resolution determines the boundary resolution for the plasma. However it is possible to supply detailed plates to refine the neutral interaction region. The HSX domain is unique with respect to other EMC3 simulation domains because the domain extends out to the wall in all directions. Other domains typically include divertor or limiter structures that protrude from the vessel wall, and the domain only extends some nominal distance into the shadowed regions of these structures.

In addition to the standard configuration, auxiliary coils can be used to break the quasi-helical symmetry and significantly alter the edge properties. Three separate magnetic configurations are considered in order to explore the role of magnetic island structures in a stellarator edge. Poincaré plots for these configurations are shown in Figure 1. The three configurations are: a standard configuration with medium sized islands, a configuration with small islands, and a configuration with large islands. The standard configuration has a LCFS that is bounded by an 8/7 island structure that intersects the wall. To make the small island configuration, current is added into the auxiliary coils which breaks the quasi-helical symmetry by a small amount. This alters the rotational transform profile, moving the 8/7 further into the edge. A 16/15 structure with very small islands is introduced between the LCFS and the 8/7 structure. It is possible to see the 8/7 resonance in both this configuration and the standard configuration in the plots

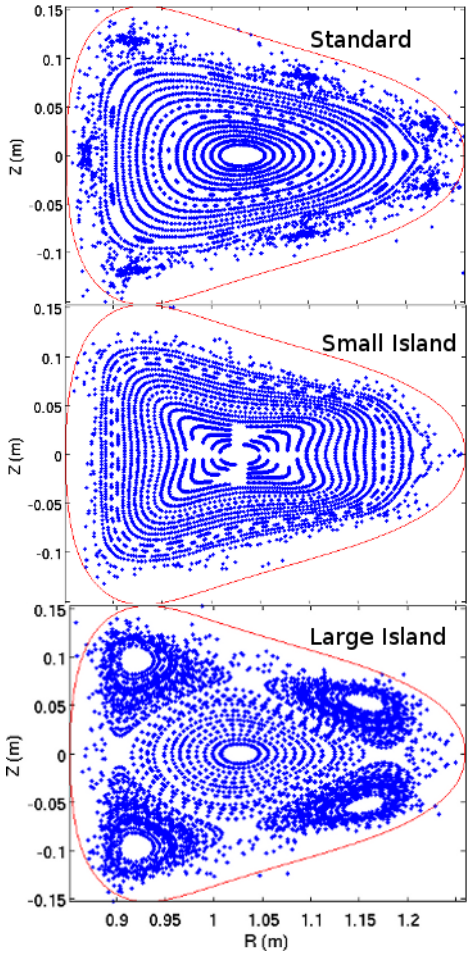

FIG. 1: Poincaré plots for standard, small island and large island configurations at the up-down symmetric toroidal cut at $\phi = \pi/4$ radians. The red line indicates the position of the vessel wall

of $n_e V_{\|}$ (see e.g. Figure 2). The 16/15 island chain is too small to be seen.

Adding more current into the auxiliary coils, drops the edge transform to 1.0 and a large 4/4 structure appears in the edge of the plasma. This is the large island configuration. These large islands dominate the edge, and the volume occupied by the main plasma is much smaller when compared to either the standard or the small island configurations. This magnetic configuration is interesting for various reasons. Each island is a separate magnetic structure. That is, field lines that begin in one island remain in that island or intersect the wall. This is different from bounding structures of the other configurations, where a single field line will map out a surface across the entire island structure. Except for the absence of divertor plates, the bounding structure of the large island configuration is similar to the 5/5 island structure at the edge of W7X.

IV. DIVERTOR REGIMES IN THE HSX GEOMETRY

Various configurations are explored by scanning upstream or separatrix densities while scaling the input power so that the power per particle is constant across the density scans. Power is input into the innermost flux surface, roughly at the plasma separatrix, and equal power is applied to both electrons and ions. For the double-sized machine, at upstream densities of 8×10^{19} m^{-3}, 24 MW of power are split evenly between electrons and ions. The input power scales linearly with density through the density scan. Unless otherwise specified, $D = 1$ m^2/s and $\chi_e = \chi_i = 3D$ are used. In these simulations, parallel viscosity is ignored (see Section IV B). Downstream parameters are calculated by taking a pressure-weighted average for the downstream parameter, Q_d, of the form,

$$Q_d = \frac{\sum_{\text{surf}} QP}{\sum_{\text{surf}} P}, \tag{7}$$

where Q is the local value of the quantity to average, P is the sum of the electron and ion pressures and the summation is taken over all volume elements adjacent to solid elements.

We keep separatrix density constant and input power constant across all three configurations, but it is difficult to make direct comparisons between the large island case and the other two cases due to the large differences in volumes occupied by the edge and the confined plasma. Nevertheless qualitative differences can be examined.

Simulation results for plasmas in the low recycling regime for all three double-sized configurations are presented in Figure 2. The standard and small island configurations have separatrix densities of 2×10^{19} m^{-3}. The large island configuration has a separatrix density of 1×10^{19} m^{-3} but reaches higher densities inside some of the edge island structures. Almost all simulations of the large island configuration show some density build-up inside the islands from neutrals ionizing on confined field lines. Separatrix temperature for both ions and electrons is roughly $\sim$200 eV for all three simulations. In all these plasmas there is a significant decrease in density but only a small decrease in temperature between the separatrix and the wall. Most of the power exiting the plasma across the separatrix is deposited on the wall by particles and is limited only by transmission through the plasma sheath.

The plots of the $n_e V_{\|}$ on the bottom row of Figures 2 and 3 best show the differences in the island structure of the three regimes. Edge flows are sourced by the Bohm boundary condition at the target. Since flows are directed towards the target on both sides of the island, they are oppositely directed with respect to the magnetic field. Near the island x-point, flows are oppositely flowing from two adjacent islands. Inside the island, flows arise due to finite perpendicular viscosity causing momentum diffusion from the island edge. If the islands are small and close, frictional

forces between the counter-streaming flows on either side of the same island, or between adjacent islands can be important.

In the high recycling regime, the edge properties are very different (Figure 3). There is a build-up of density near the plasma-wall interaction region. For the flux surface shown, this buildup is seen most strongly in the inboard side at the tops and bottoms and to a lesser extent at the outboard midplane. The separatrix densities are 1.2×10^{20} m^{-3} for the standard and small island simulations and 8.0×10^{19} m^{-3} for the large island configuration. It should be remarked that the transition densities into the high recycling regime are higher than what has been experimentally obtainable in stellarators of comparable size. Separatrix temperature is roughly 200 eV for all three simulations. For all three configurations roughly 10-25% of the power is lost to radiative processes, although impurities were not included. Both ion and electron temperatures at the wall range from 10-20 eV for the three configurations (see Table I).

Plots of n_d/n_u as a function of upstream density for different configurations are shown in Figure 4. From these plots it can be seen that in the range of densities simulated, all three configurations of the large size devices transitioned to the high recycling regime. A signature of the transition is when n_d/n_u is above one. Using this criteria, the large size, large island configuration transitions to a high recycling regime at an upstream density of $\sim 2.0 \times 10^{19}$. The two other configurations in the large size device and the large island configuration in the small device transition at upstream densities between 6.0 and 8.0×10^{19}. n_u is calculated as the density at the innermost flux surface and is usually very similar to the separatrix density. n_d is calculated by taking a pressure-weighted average over the boundary, as described above (Eq. 7). Only the large island configuration transitions into a high recycling regime for the normal HSX size, and generally displays markedly different behavior from the other two configurations. Again it is important to note that a quantitative comparison between the configurations is made difficult by the fact that the volume occupied by the confined plasma is very different between the large island configuration and the other two.

Somewhat surprisingly, there is little noticeable difference between the standard configuration and the small island, configuration with respect to high recycling transitions. This occurs despite the differences in magnitude of the flows associated with the 8/7 structure. There are several possible explanations. In the small island case, the largest values of $n_e V_\parallel$ occur near the three strike points. In these regions counter-streaming flows are visible and are of comparable magnitude to those in the standard case. These are shown in detail in the top plot of Figure 5. It is possible that the interactions in this region are the dominant forces in the edge behavior for both configurations. Another possibility is analogous to that found in LHD, where friction arises from counter-streaming flows found in radially separated island

chains of different poloidal numbers. Often these interacting regions can be very large, compensating for the fact that the flow magnitude is smaller. In the small island case additional resonant structures appear and these may provide enough friction to modify the edge momentum transport. The additional structures are shown in the bottom plot of Figure 5, where additional flow structures inside the edge island chain are visible.

Nevertheless, it appears from Figure 4 that the large island configuration provides favorable divertor qualities, transitioning to a high recycling region at a lower upstream density for a given amount of input power. This is in qualitative agreement with simulations on W7-AS and W7X which concluded that the perpendicular scale length increases with island size and mitigates the contribution from the cross-field transport in the momentum balance equation. However, there is reason for caution in interpreting these results as favoring a reactor geometry similar to the large island configuration. First, these simulations are calculated assuming that there is no plasma contribution to the magnetic field, and the vacuum field is the sole important field. Admittedly, this is a poor assumption, so the results are really dependent on the ability to impose the magnetic configuration in the presence of finite-β and plasma flows. The second drawback is more obvious. The large island configuration has a much smaller core plasma region than the other two configurations. The islands, which are in general colder than the core plasma, take up much of the room in the vacuum vessel. In reality, there is a trade-off between the size of the edge islands and the core plasma, with larger islands providing for better power exhaust to the wall but leaving less room for a fusing plasma. Nevertheless, the large island configurations provides opportunities to examine the role of large islands in the edge of a QHS device.

A. Varying the Diffusion Coefficients

The physical mechanism and the magnitude of the perpendicular diffusion in the edge of both tokamak and stellarator plasmas is not known. The simulations presented so far assume perpendicular diffusion and viscosity coefficient values of $D = \mu_\perp = 1$ m^2/s. The effects of lowering $D, \mu_\perp$ and χ by a factor of 4 to $D = \mu_\perp = 0.25$ m^2/s are explored. As before, $\chi_{i,e} = 3D$, and the total power injected into the plasma is constant.

Reducing D and χ contracts the channels that carry heat flux to the wall. The wetted area where heat flux intersects the wall is reduced. For these simulations, the resulting reduction in wetted area is highly dependent on magnetic geometry. However, a decrease in $\mu_\perp$ also reduces the magnitude of the cross-field transport in Eq 4. This will produce behavior closer to that expected from the two-point model [10]. In other words, density at the wall should go up as perpendicular diffusion decreases.

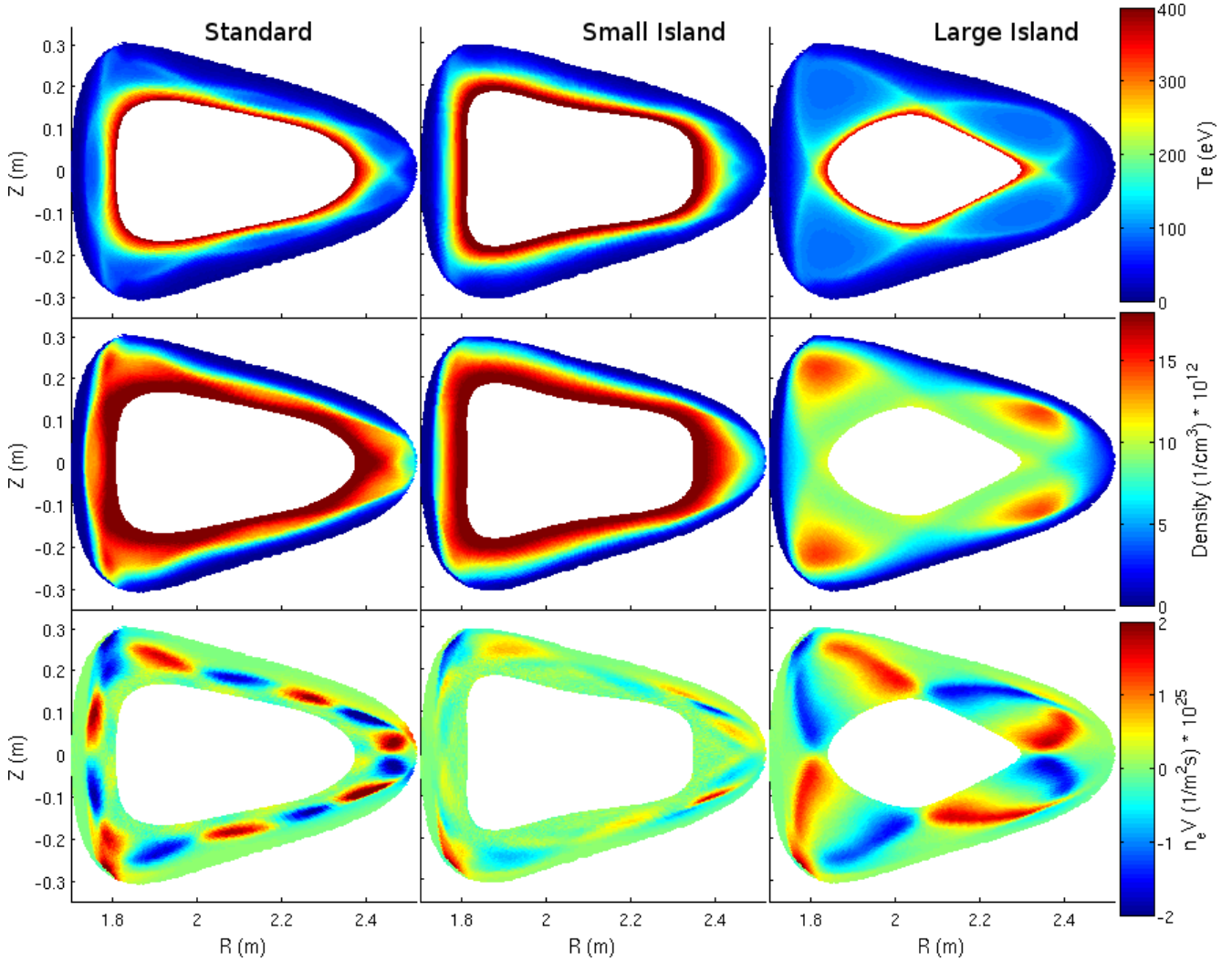

FIG. 2: Low recycling regime plots of T_e (top) $n_e = n_i$ (middle) and ion flow ($n_e V_{i,\|}$) (bottom) for standard (left) small island (middle) and large island (right) configurations.

This is precisely the behavior that is seen in the small island configuration. The ratio of $P_{\rm rad}$ to $P_{\rm tot}$ remains roughly the same, but the power is deposited over a much smaller wetted area. The contraction occurs in the poloidal direction, as might be expected from a comparison with tokamaks, but also in the toroidal direction, which is unique to the 3D stellarator geometry. This yields both higher densities and higher peak temperatures at the wall (Figure 6). The higher densities arise from the reduction of the perpendicular viscosity in the parallel momentum equation yielding a result more akin to a high recycling regime, and the higher temperatures arise from a reduction in the width of the heat flux deposition.

Similar behavior is seen in the standard case, however a much more modest temperature rise at the wall is seen. This is in agreement with a much smaller toroidal localization of the heat flux.

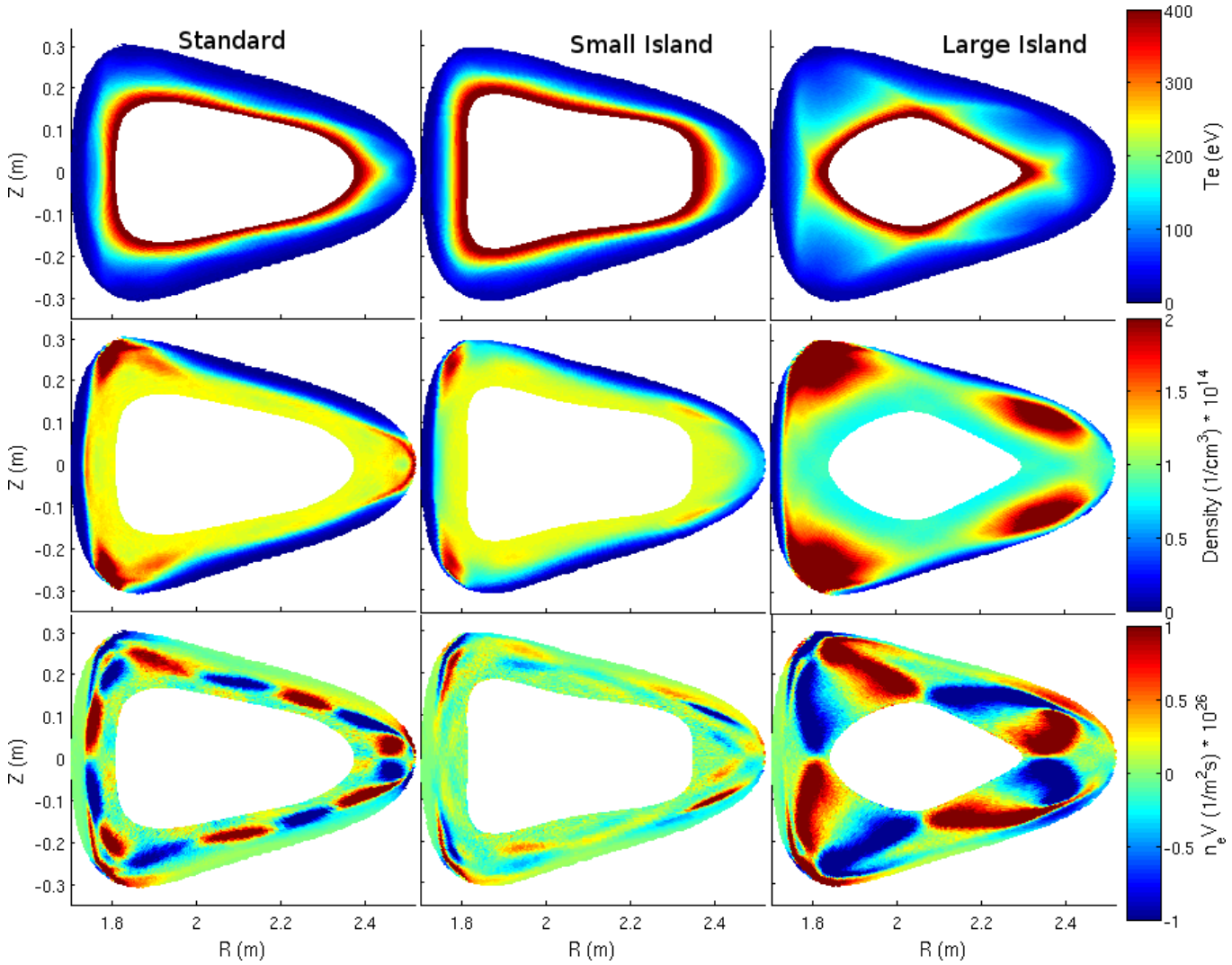

FIG. 3: High recycling regime plots of T_e (top) $n_e = n_i$ (middle) and ion flow ($n_e V_{i,\|}$) (bottom) for standard (left) small island (middle) and large island (right) configurations.

The large island case has very different behavior. The downstream density rises only slightly, but the relative increase in downstream temperature is similar to that of the small island configuration. The divergence of expected behavior arises from the peculiarities of the large island configuration. In a simplified model, both particles and heat flux can be transported either through an island by cross-field transport or around an island following field lines with possibly long connection lengths. Particle transport time through an island is approximately $t_\perp = \Delta^2/D$, where Δ is the width of the island. Particle transport around an island edge is approximately $t_\| = \pi R_0/m\iota'\Delta v_t$, where R_0 is the major radius, v_t is the thermal speed, m is the poloidal island number, and ι' represents the internal island shear, that is, $m\iota'\Delta$ represents the number of poloidal transits around an island for one toroidal transit through the device. Therefore $\pi R_0/m\iota'\Delta$ is the distance along a field line a particle would need to travel in order to traverse from

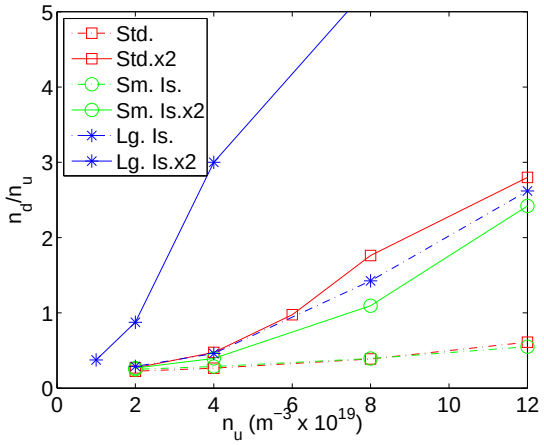

FIG. 4: Plots of the ratio of downstream vs upstream densities (n_d/n_u) vs n_u (at constant P/n) for standard (red squares), small islands (green circles) and large islands (blue stars) at both normal (dash dot) and double (solid) sizes. The red and green dash-dot lines overlap for most of the range.

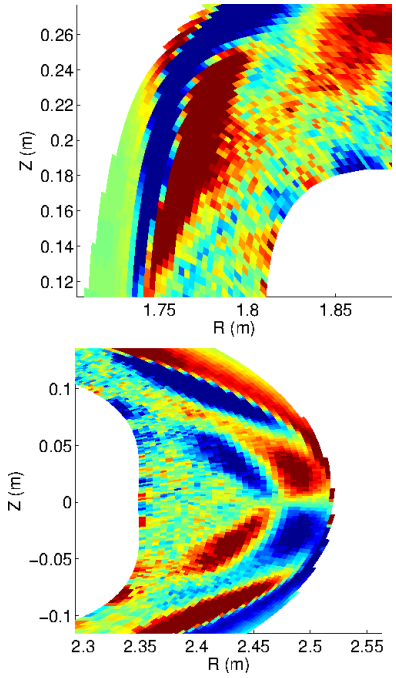

FIG. 5: Zoomed in plots of $n_e V_{i,\|}$ for the small island configuration with enhanced contrast. The top plot shows the location near the strike point on the upper inboard side. The bottom plot shows additional island structures in addition to the 8/7 structure on the outboard midplane.

the edge of the island near the inboard side to the edge near the outboard side. The condition for parallel transport around an island to be dominant is,

$$\frac{t_\|}{t_\perp} \approx \frac{\pi R_0}{m\iota' v_t \Delta^3} D \ll 1 \tag{8}$$

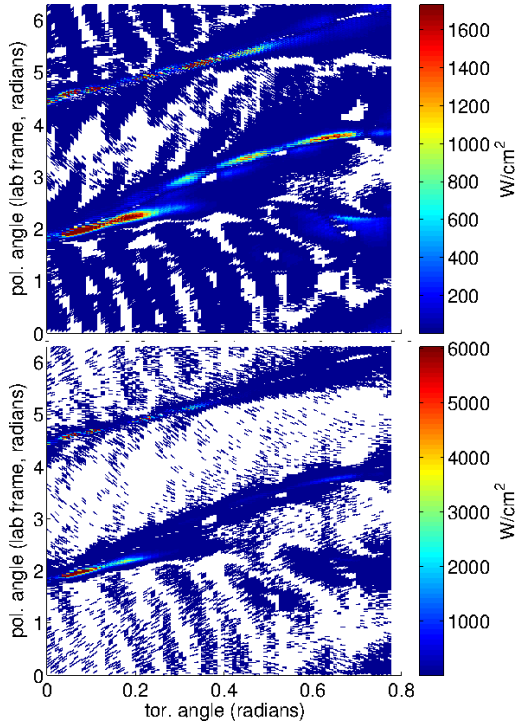

FIG. 6: Comparison of the power deposition for the small island configuration for $D = 1$ m^2/s (top) and $D = 0.25$ m^2/s (bottom). The poloidal angle is calculated in the lab frame. Areas with no calculated flux deposition are left white.

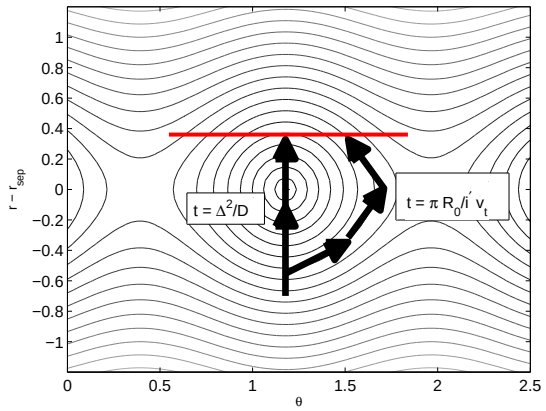

FIG. 7: Illustration of the particle transport paths through and around an island, and ending on a target plate (red line)

The respective paths are illustrated in Figure 7. In the standard case with small islands $m\iota' \approx 1/7$, $\Delta \approx 2$ cm and $R_0 = 2.4$ m for the double-sized HSX giving a value of $t_\parallel/t_\perp$ of $\sim$1.3 D for a 50 eV hydrogen ion (D in m^2/s). In this case, both transport through and around an island are competitive, so large differences in the momentum transport behavior are expected with variations in D. However, in the large island configuration the islands are larger but $m\iota'$

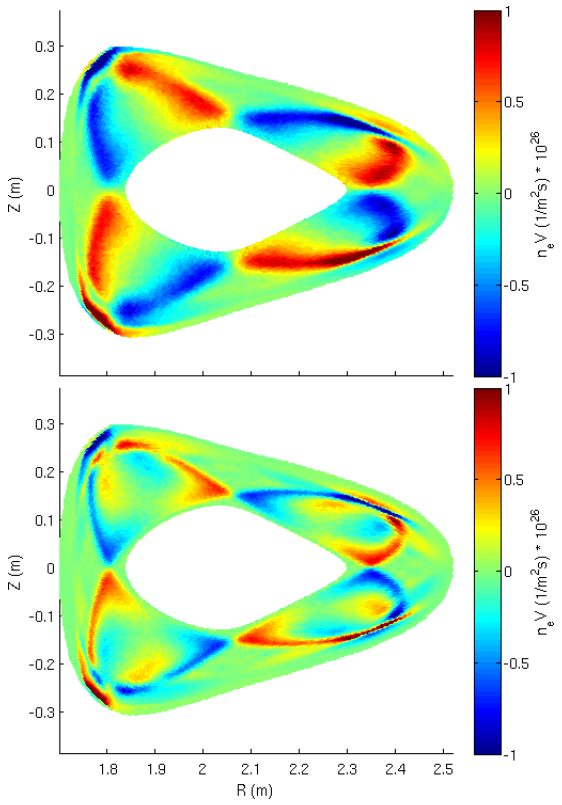

FIG. 8: Comparison on $n_e V_{||}$ for a large island simulation with $D = 1$ m^2/s (top) and $D = 0.25$m^2/s (bottom).

is smaller. Using $\Delta \approx 10$ cm and $m\iota' \approx 1/24$ in the island edge, yields $t_{||}/t_{\perp} \approx 0.2D$. In this case a reduction of D will not affect the transport greatly because transport on parallel lines around the plasma is dominant for both values of D that were considered.

Another aspect of the viscosity coefficient is that a larger value of $\mu_{\perp}$ tends to smear out flow structures in the islands. Smaller values of $\mu_{\perp}$ produce sharper and smaller structures due to the lack of coupling between the edge and core of the island. This is shown in Figure 8, where $n_e V_{||}$ for two large island simulations are compared. These simulations have all the same parameters except that the bottom figure has $\mu_{\perp} = 0.25$ m^2/s and the top has $\mu_{\perp} = 1$ m^2/s. The lower $\mu_{\perp}$ simulation shows a much sharper flow structure that is confined to the edges of the islands.

B. Validity of Collisional Parallel Viscosity

The simulation results presented so far are all taken ignoring any momentum loss from parallel velocity. I.e $\eta_{||} = 0$ in Eq. 4. A collisional treatment for parallel viscosity is only valid when the typical collisional length, λ_c, is short compared to the parallel scale length, $x_{||}$. In low collisionality plasmas, Braginskii parallel viscosity becomes very

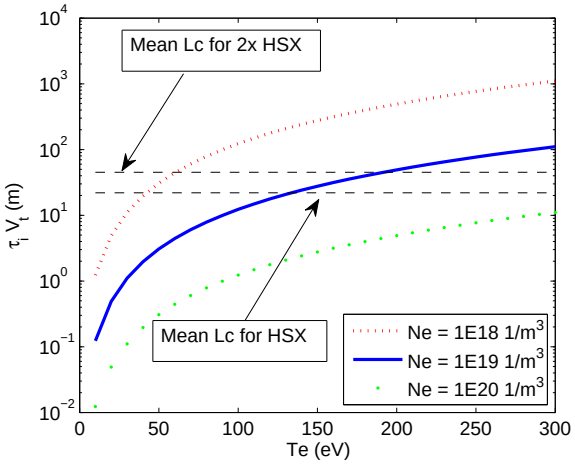

FIG. 9: Estimation of collisional length plotted against T_e for various plasma density values.

large and can result in an unphysical force on the plasma flow [11]. Properly accounting for the low collisionality by providing a proper closure moment, reduces the effect of parallel viscosity on pressure balance significantly.

An improved model for parallel viscosity is beyond the scope of this paper. Instead calculations of λ_c and $x_{\|}$ are used to determine whether parallel viscosity is likely to produce an unphysical result. For $x_{\|}$ some information on field line connection lengths are needed. A typical field line started 0.5 cm outside the separatrix reaches the wall in approximately 20 m for the double sized HSX device in the standard configuration. There are field lines with very long (up to 250 m) and very short (1-2 m) connection lengths, but the mean value for the target-to-target connection length is roughly 2 $\times$ the average upstream-to-wall value, or approximately 40 m.

Collision lengths are plotted vs. temperature for three edge density values in Figure 9. These plots show that a collisional treatment of viscosity is valid solely for plasmas with low temperature and high density. In the simulation results, it is found that setting parallel viscosity to the classical value increases n_d by factors of 2 or more at low densities. At higher densities the viscosity provides roughly a 10-20% increase. We conclude that including a collisional description of parallel viscosity is responsible for an unphysical increase in the n_d for the lowest density plasmas, but is probably valid for the highest density plasmas. Nevertheless, for consistency, parallel viscosity is not included in any of the simulations shown in this paper.

C. Addition of Carbon Impurities

In addition to the plasma species, EMC3-EIRENE can also solve for impurity species in the plasma, which is necessary for determining the transition to detached regimes [7]. EMC3-EIRENE solves for each ionization stage of

a given impurity species using,

$$\nabla\cdot\left(n_I^z V_{I,\parallel}^z \vec{b} - D_I^z \vec{b}_\perp \vec{b}_\perp \cdot \nabla n_I^z\right) = S_{z-1\to z} - S_{z\to z+1} + R_{z+1\to z} - R_{z\to z-1}, \tag{9}$$

$$U_{I,i}^z\left(V_{I,\parallel}^z - V_{i,\parallel}\right) = -\vec{b}\cdot\nabla n_I^z T_i + n_I^z Z e E_\parallel + n_I^z Z^2 C_e \vec{b}\cdot\nabla T_e + n_I^z C_i \vec{b}\cdot\nabla T_i. \tag{10}$$

In the above equations, n_I^z and $V_{I,\parallel}^z$ are the impurity density and parallel flow velocity, respectively. The S terms represent ionization and the R terms represent recombination processes. $U_{I,i}^z$ is the ion-impurity friction coefficient the ion-impurity friction and $E_\parallel$, the parallel electric field, is calculated from parallel momentum balance. EMC3 sources impurities using, $\Gamma_I = Y_I\Gamma_i$, the flux of impurities into the plasma at a target is directly proportional to the ion flux to the target with a user-set multiplication factor Y_I representing a sputtering coefficient. This ad-hoc model mimics chemical sputtering, a process that is not dependent on the incoming ion energy, and one that is dominant at low ion temperature. For all simulations in this paper $Y_I = 0.03$, a value in the range used for W7-AS simulations [9].

Impurities in the core of a plasma radiate more strongly than the lower Z fusing species and are deleterious to good plasma performance. However, the same process causes impurities to have a beneficial role in the edge. Namely, they improve the fraction of the power radiated. Because impurities cause a higher radiated power fraction in the edge, their inclusion in the simulation is important for determining when the plasma achieves detachment. It should be noted that EMC3-EIRENE only allows ions to neutralize at the wall, so no volume recombination processes are included. Recombination should become more important as the edge neutral density increases. Therefore, it is expected that the power flux to the wall to be overestimated in highly radiated plasmas.

Direct comparisons between simulations with and without impurities are made for plasmas in the high recycling regime. The fraction of radiated power to power deposited on the wall, α_{rad}, with and without impurities are shown below in Table I.

In the standard configuration, the addition of impurities does not radiate enough power to transition into a detached regime, while the large island case reaches almost 90% radiated power. The radiation fraction along with a reduction of downstream electron temperature suggest partial detachment.

Config.	$\mathbf{n_u}$ (m^{-3})	T_d (keV) (w/o. Imp.)	α_{rad} (w/o. Imp.)	T_d (keV) (w/ Imp.)	α_{rad} (w/ Imp.)
Standard	8×10^{19}	23.5	0.09	18.5	0.29
Large island	4×10^{19}	15.9	0.13	8.1	0.73
Large island	8×10^{19}	9.0	0.23	4.8	0.89

TABLE I: Downstream (electron) temperatures and radiated power fractions for simulations with and without impurities.

V. CONCLUSION

The EMC3-EIRENE code has been successfully implemented on the HSX geometry and used to explore various magnetic configurations with different edge properties. These results represent a probing study for the use of EMC3-EIRENE on HSX-like geometries with the aim of predicting behavior for future stellarator designs. The simulations examine three magnetic of interest to HSX where the distinguishing feature is the presence and size of magnetic island structures in the edge region.

Overall, larger island sizes and lower cross-field transport coefficients values yield more tokamak-like behavior with regard to momentum transport. This is caused by the dominant transport path being around the edge islands with path length $\pi R/m\iota'\Delta$ and suffering minimal effects from cross-field transport. Large differences are seen between the edge behavior of the large island magnetic configuration where the edge is dominated by a large 4/4 island structure, and the standard and small island configuration where the edges are dominated by smaller island structures.

The large island configuration reaches a high recycling regime at lower separatrix densities and temperatures than the other two configurations. However, when impurities are added the plasma transitions into a detached regime. The other configurations do not transition into a detached regime even at high densities. There is little noticeable difference in performance between the small island case and the standard case, and the reason for this is currently not fully known.

The results highlight the trade-offs that exist in edge divertor design. Large islands are desirable for their propensity to transition to better divertor regimes at lower separatrix densities, but suffer from a reduction in fusing plasma volume and require tight control over the plasma current to ensure that the edge structures remain in the desired locations during the startup and flattop phases of the plasma. Smaller edge structures leave more room for a core fusing plasma, but generally have poorer edge performance.

Acknowledgments

This work supported by U.S. Department of Energy under grant USDOE-SC0006103

[1] R. König, P. Grigull, K. McCormick, Y. Feng, J. Kisslinger, A. Komori, S. Masuzaki, K. Matsuoka, T. Obiki, N. Ohyabu, et al., Plasma Physics and Controlled Fusion **44**, 2365 (2002), URL http://stacks.iop.org/0741-3335/44/i=11/a=306.

[2] N. Ohyabu and H. Renner, Contributions to Plasma Physics **38**, 94 (1998), ISSN 1521-3986, URL http://dx.doi.org/10.1002/ctpp.2150380114.

[3] P. Grigull, K. McCormick, J. Baldzuhn, R. Burhenn, R. Brakel, H. Ehmler, Y. Feng, F. Gadelmeier, L. Giannone, D. Hartmann, et al., Plasma Physics and Controlled Fusion **43**, A175 (2001), URL http://stacks.iop.org/0741-3335/43/i=12A/a=313.

[4] H. Renner, J. Boscary, V. Erckmann, H. Greuner, H. Grote, J. Sapper, E. Speth, F. Wesner, M. Wanner, and W.-X. Team, Nuclear Fusion **40**, 1083 (2000), URL http://stacks.iop.org/0029-5515/40/i=6/a=306.

[5] N. Ohyabu, T. Watanabe, H. Ji, H. Akao, T. Ono, T. Kawamura, K. Yamazaki, K. Akaishi, N. Inoue, A. Komori, et al., Nuclear Fusion **34**, 387 (1994), URL http://stacks.iop.org/0029-5515/34/i=3/a=I07.

[6] A. Komori, T. Morisaki, S. Masuzaki, M. Kobayashi, Y. Feng, M. Shoji, N. Ohyabu, K. Ida, K. Tanaka, K. Kawahata, et al., Nuclear Fusion **45**, 837 (2005), URL http://stacks.iop.org/0029-5515/45/i=8/a=009.

[7] Y. Feng, F. Sardei, J. Kisslinger, P. Grigull, K. McCormick, and D. Reiter, Contributions to Plasma Physics **44**, 57 (2004), ISSN 1521-3986, URL http://dx.doi.org/10.1002/ctpp.200410009.

[8] F. Anderson, A. Almagri, D. Anderson, P. Matthews, J. Talmadge, and J. Shohet, Fusion Science and Technology **17**, 273 (1995).

[9] Y. Feng, F. Sardei, P. Grigull, K. McCormick, J. Kisslinger, D. Reiter, and Y. Igitkhanov, Plasma Physics and Controlled Fusion **44**, 611 (2002), URL http://stacks.iop.org/0741-3335/44/i=5/a=308.

[10] Y. Feng, M. Kobayashi, T. Lunt, and D. Reiter, Plasma Physics and Controlled Fusion **53**, 024009 (2011), URL http://stacks.iop.org/0741-3335/53/i=2/a=024009.

[11] P. Stangeby, *The Plasma Boundary of Magnetic Fusion Devices* (Bristol: Institute of Physics Publishing, 2000).

[12] Y. Shimomura, M. Keilhacker, K. Lackner, and H. Murmann, Nuclear Fusion **23**, 869 (1983), URL http://stacks.iop.org/0029-5515/23/i=7/a=002.

[13] A. Loarte, R. Monk, J. Martn-Sols, D. Campbell, A. Chankin, S. Clement, S. Davies, J. Ehrenberg, S. Erents, H. Guo, et al., Nuclear Fusion **38**, 331 (1998), URL http://stacks.iop.org/0029-5515/38/i=3/a=303.

[14] B. Labombard, J. Goetz, I. Hutchinson, D. Jablonski, J. Kesner, C. Kurz, B. Lipschultz, G. McCracken, A. Niemczewski,

J. Terry, et al., Journal of Nuclear Materials **241243**, 149 (1997), ISSN 0022-3115, URL http://www.sciencedirect.com/science/article/pii/S0022311597800372.

[15] Y. Feng, M. Kobayashi, T. Morisaki, S. Masuzaki, J. Miyazawa, B. Peterson, S. Morita, M. Shoji, K. Ida, I. Yamada, et al., Nuclear Fusion **48**, 024012 (2008), URL http://stacks.iop.org/0029-5515/48/i=2/a=024012.

[16] Y. Feng, M. Kobayashi, F. Sardei, S. Masuzaki, J. Kisslinger, T. Morisaki, P. Grigull, H. Yamada, K. McCormick, N. Ohyabu, et al., Nuclear Fusion **49**, 095002 (2009), URL http://stacks.iop.org/0029-5515/49/i=9/a=095002.

[17] J. R. Myra, D. A. Russell, D. A. D'Ippolito, J.-W. Ahn, R. Maingi, R. J. Maqueda, D. P. Lundberg, D. P. Stotler, S. J. Zweben, J. Boedo, et al., Physics of Plasmas **18**, 012305 (pages 12) (2011), URL http://link.aip.org/link/?PHP/18/012305/1.

[18] R. Goldston, Nuclear Fusion **52**, 013009 (2012), URL http://stacks.iop.org/0029-5515/52/i=1/a=013009.

[19] Y. Feng, F. Sardei, J. Kisslinger, P. Grigull, K. McCormick, D. Reiter, L. Giannone, R. Knig, N. Ramasubramanian, H. Thomsen, et al., Nuclear Fusion **45**, 89 (2005), URL http://stacks.iop.org/0029-5515/45/i=2/a=003.

[20] Y. Feng, F. Sardei, and J. Kisslinger, Physics of Plasmas **12**, 052505 (pages 7) (2005), URL http://link.aip.org/link/?PHP/12/052505/1.

[21] T. Morisaki, S. Masuzaki, A. Komori, N. Ohyabu, M. Kobayashi, Y. Feng, F. Sardei, K. Narihara, K. Tanaka, K. Ida, et al., Journal of Nuclear Materials **337339**, 154 (2005), ISSN 0022-3115, ¡ce:title¿PSI-16¡/ce:title¿, URL http://www.sciencedirect.com/science/article/pii/S0022311504009778.

[22] H. Frerichs, D. Reiter, O. Schmitz, P. Cahyna, T. E. Evans, Y. Feng, and E. Nardon, Physics of Plasmas **19**, 052507 (pages 7) (2012), URL http://link.aip.org/link/?PHP/19/052507/1.

[23] H. Frerichs, M. Clever, Y. Feng, M. Lehnen, D. Reiter, and O. Schmitz, Nuclear Fusion **52**, 023001 (2012), URL http://stacks.iop.org/0029-5515/52/i=2/a=023001.

[24] T. Lunt, Y. Feng, M. Bernert, A. Herrmann, P. de Marn, R. McDermott, H. Mller, S. Potzel, T. Ptterich, S. Rathgeber, et al., Nuclear Fusion **52**, 054013 (2012), URL http://stacks.iop.org/0029-5515/52/i=5/a=054013.

[25] J. Lore, J. Canik, Y. Feng, J.-W. Ahn, R. Maingi, and V. Soukhanovskii, Nuclear Fusion **52**, 054012 (2012), URL http://stacks.iop.org/0029-5515/52/i=5/a=054012.

[26] C. Hegna, Nuclear Fusion **51**, 113017 (2011), URL http://stacks.iop.org/0029-5515/51/i=11/a=113017.

[27] C. C. Hegna, Physics of Plasmas **19**, 056101 (pages 8) (2012), URL http://link.aip.org/link/?PHP/19/056101/1.